DESY 15-028 ISSN
23.02.2015

A Quartz Cherenkov Detector for Compton-Polarimetry at Future e^+e^- Colliders

Jenny List[1], Annika Vauth[1,2], and Benedikt Vormwald[1,2]

1- Deutsches Elektronen-Synchrotron DESY
Notkestr. 85, 22607 Hamburg, Germany

2- Universität Hamburg, Institut für Experimentalphysik
Luruper Chaussee 149, 22761 Hamburg, Germany

Abstract

Precision polarimetry is essential for future e^+e^- colliders and requires Compton polarimeters designed for negligible statistical uncertainties. In this paper, we discuss the design and construction of a quartz Cherenkov detector for such Compton polarimeters. The detector concept has been developed with regard to the main systematic uncertainties of the polarisation measurements, namely the linearity of the detector response and detector alignment. Simulation studies presented here imply that the light yield reachable by using quartz as Cherenkov medium allows to resolve in the Cherenkov photon spectra individual peaks corresponding to different numbers of Compton electrons. The benefits of the application of a detector with such single-peak resolution to the polarisation measurement are shown for the example of the upstream polarimeters foreseen at the International Linear Collider. Results of a first testbeam campaign with a four-channel prototype confirming simulation predictions for single electrons are presented.

1 Introduction

Polarised beams are a key ingredient of the physics program of future electron-positron colliders [1]. The precise knowledge of the beam polarisation is as important as the knowledge of the luminosity, since for electroweak processes, the absolute normalisation of expected event rates depends on both quantities to the same order. The values relevant for the experiments, namely the luminosity-weighted average polarisations at the interaction point $\langle\mathcal{P}\rangle_{\text{lumi}}$, have to be determined by combining fast measurements of Compton polarimeters with long-term scale calibration obtained from reference processes in collision data.

In particular for the International Linear Collider [2], where both beams are foreseen to be longitudinally polarised, it is required to control $\langle\mathcal{P}\rangle_{\text{lumi}}$ with permille-level precision. Two Compton polarimeters [3] per beam aim to measure the longitudinal polarisation before and after the collision with a precision of $\delta\mathcal{P}/\mathcal{P} \leq 0.25\%$[1]. It should be noted, though, that this goal is not driven by physics requirements, but by what used to be considered feasible experimentally. Thus, further improvements in polarimetry would still have direct benefits for the physics potential of the machine. Spin tracking simulations are required to evaluate the effects on the mean polarisation vector caused by the beamline magnets between the polarimeters and the interaction point, by the detector magnets and by the beam-beam interaction. These effects have recently been studied in [8], concluding that a cross-calibration of the polarimeters to 0.1 % is feasible, as well as individual extrapolations of upstream and downstream measurements to the e^+e^- interaction point.

The long-term average of the polarisation at the interaction point can be determined from reference reactions, where in particular W pair production [4–6] and single W production [7] have been studied. Precisions of about 0.15% can be achieved after several years of data taking. Any imperfection in the beam helicity reversal, i.e. differences in the magnitude of the polarisation between measurements with left- and right-handed polarised beams, has to be corrected for based on the polarimeter measurements.

The two polarimeters are located about 1.8 km upstream and 160 m downstream of the interaction point. Both provide non-destructive measurements of the longitudinal beam polarisation based on the polarisation dependence of Compton scattering and have been designed for operation at beam energies between 45 GeV and 500 GeV. In the order of 10^3 electrons[2] per bunch undergo Compton scattering with circularly polarised laser light which is shot under a small angle onto individual bunches. The energy spectrum of these scattered particles depends on the product of laser and beam polarisations as shown in figure 1a, and the differential rate asymmetry with respect to the sign of the circular laser polarisation λ is directly proportional to the beam polarisation. The asymmetry expected for $\lambda\mathcal{P} = 100\%$ is called analysing power $\mathcal{A}\mathcal{P}$. The scattering angle in the laboratory frame is less than 10 μrad, so that a magnetic chicane is employed to transform the energy spectrum into a spatial distribution. Such a spatial distribution is shown in figure 1b for the example of the chicane foreseen for the ILC's upstream polarimeters, which is sketched in figure 1c.

[1] for typical ILC beam polarisation values of $\mathcal{P}_{e^-} \geq 80\%$ and $\mathcal{P}_{e^+} \geq 30\%$ or even $\geq 60\%$.

[2] or positrons in case of the positron beam of the ILC which is equipped analogously.

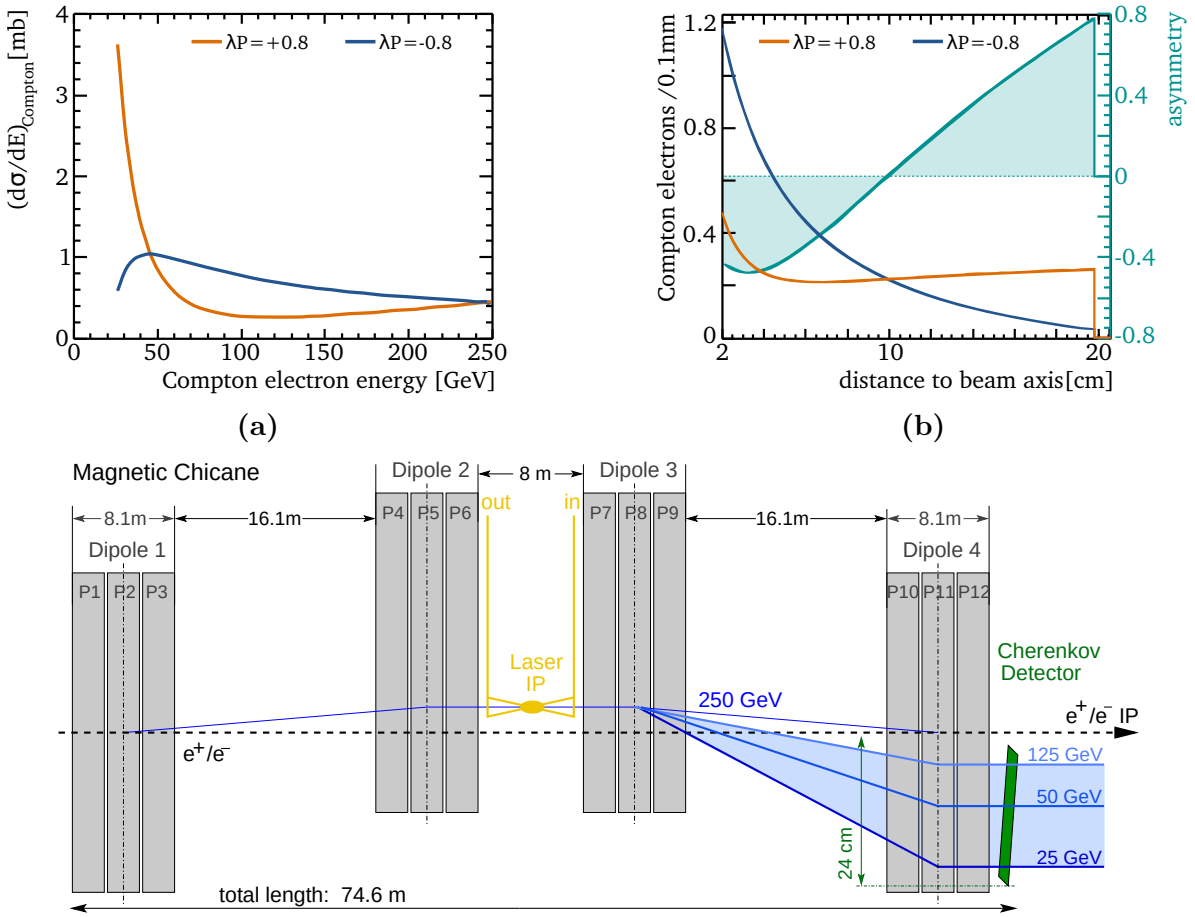

Figure 1: (a) Differential cross-section in dependence of the energy of the scattered electron for $\lambda\mathcal{P} = \pm 80\,\%$. (c) Sketch of the magnetic spectrometer for the ILC upstream polarimeter (from [9]). The Compton-scattered electrons with the lowest energies are deflected most by the spectrometer. (b) Spatial distribution of the Compton scattered electrons at the detector location behind the magnetic chicane for $\lambda\mathcal{P} = \pm 80\%$. The filled area indicates the resulting asymmetry (secondary y-axis).

Several options for detecting the Compton-scattered electrons behind the last magnet of the chicane are being considered. The baseline solution is a gas Cherenkov detector consisting of 20 channels, each 1 cm wide. The rate asymmetry $\mathcal{A}_i$ with respect to the laser helicity is determined in each channel i as

$$\mathcal{A}_i = \frac{N_i^R - N_i^L}{N_i^R + N_i^L}, \tag{1}$$

where N_i^R and N_i^L are the count rates in channel i for right- and left-handed laser polarisation, respectively.

Per-channel measurements of the beam polarisation are then obtained by comparison with the predicted analysing power $\mathcal{AP}_i$ of the corresponding channel. The predictions of $\mathcal{AP}_i$

are based on the well calculable cross-section for Compton scattering [3] plus a Monte-Carlo modelling of the magnetic chicane and the detector geometry and response. The resulting per-channel polarisation measurements are then combined in a weighted average, where the largest weights w_i are given to the channels with the smallest statistical uncertainties, which is equivalent to the channels with the largest analysing power [11]:

$$w_i = \frac{1}{(\mathcal{P} \cdot \mathcal{A}\mathcal{P}_i)^{-2} - 1} \tag{2}$$

This measurement principle has already been used successfully at the SLC polarimeter, which was the up to now most precise Compton polarimeter, reaching $\delta\mathcal{P}/\mathcal{P} = 0.5\%$ [12]. The gas Cherenkov approach is robust against high data rates, a harsh radiation environment, and possible backgrounds. The basic detection mechanism is intrinsically proportional to the number of electrons passing a single channel simultaneously, since the amount of emitted Cherenkov radiation does not depend on the energy of the particles once they are relativistic. The main source of non-linear behaviour are thus the photodetectors. Table 1 shows the anticipated uncertainty budget for the ILC Compton polarimeters assuming a Cherenkov detector, and compares it to the uncertainties achieved at the SLC polarimeter.

source of uncertainty	$\delta\mathcal{P}/\mathcal{P}$	
	SLC achieved	ILC goals
laser polarisation	0.1 %	0.1 %
detector alignment	0.4 %	0.15 % – 0.2 %
detector linearity	0.2 %	0.1 %
electronic noise and beam jitter	0.2 %	0.05 %
Total	0.5 %	0.25 %

Table 1: Uncertainty goals for the polarisation measurement at the ILC [8]. For comparison, the systematic uncertainties determined for the SLC polarimeter are also given [12].

The most challenging improvement has to be achieved with respect to the detector linearity. In order to reach the goal of not more than 0.1% contribution from this source to $\delta\mathcal{P}/\mathcal{P}$, non-linearities have to be monitored and corrected for at the level of a few permille [13]. A corresponding calibration system has been developed recently [14], matching a prototype of a gas Cherenkov detector which has been successfully operated in testbeam. With this prototype, the alignment requirement has nearly been reached and electronic noise was found to be at a negligible level [9]. The influence of beam jitter will also be much smaller in the ILC case, since the whole accelerator has been designed to limit the transverse jitter to smaller than 10% of the beam sizes [2] in order to achieve the design luminosities. Thus, it seems feasible to reach the envisaged precision goal with the baseline design.

The effect of non-linearities would be eliminated completely if the Compton-scattered electrons could be detected individually, e.g. by a Silicon Pixel detector, which would also

[3] With radiative corrections of less than 0.1% currently calculated to the order of α^3 [10].

increase significantly the possibilities to control the alignment. Here however, R&D is still required to reach a proof-of-principle level, where the main concern is the high local data rate, followed by radiation issues. Employing pixel detectors would enable in addition the measurement of transverse beam polarisation [15].

An alternative Cherenkov detector concept which promises a significant reduction of the effects of non-linearities and misalignments is the subject of this paper. It is organised as follows: In section 2, the concept of polarimetry with Compton electron counting is introduced and its benefits are demonstrated using the example of the upstream polarimeter of the International Linear Collider. Section 3 discusses the design of a suitable detector matching the requirements and introduces a corresponding prototype. In section 4, we present results from operating this prototype in testbeam before concluding in section 5.

2 Polarimetry with Compton electron counting

The detector concept discussed in this paper aims to resolve individual Compton electron peaks in the detected and digitised spectrum of the Cherenkov light. This would allow to build a "self-calibrating" detector: by determining the distance between these peaks, the gain of the photodetectors could be monitored in-situ. Even better, the shape of such a spectrum could be exploited to directly determine the number of Compton electrons in this channel for the calculation of the polarisation asymmetry, without the need to calibrate the photomultiplier gain. In this section, we will explain this concept and evaluate its potential benefit on polarimetry.

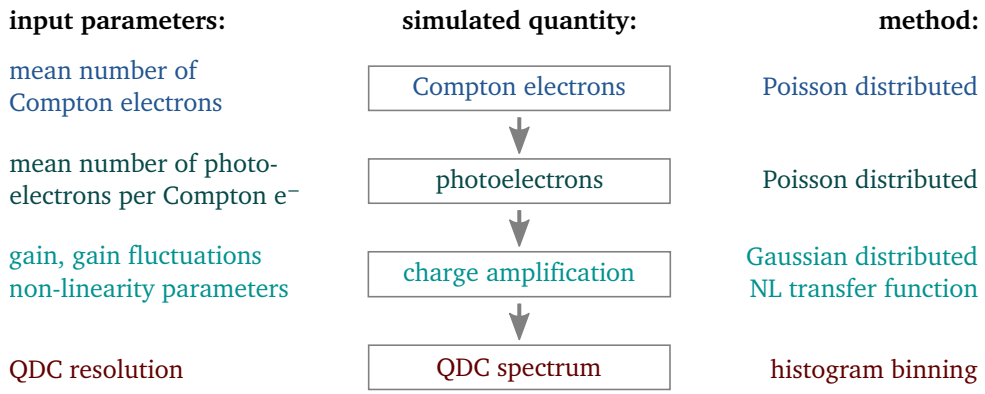

Figure 2: Schematic overview of the Monte Carlo simulation predicting the digitised detector response, with the input parameters for each simulation step in the left column and the method to implement the corresponding statistical effects in the right column.

A dedicated Monte-Carlo simulation has been developed to predict the digitised photomultiplier response for a given average number of Compton electrons per detector channel. As illustrated in figure 2, the simulation starts by determining the actual number of Compton electrons per channel based on a Poissonian distribution around the mean value. For each Compton electron, the actual number of photoelectrons created and emitted from the

photocathode of a photomultiplier is determined, again assuming Poissonian statistics[4]. The charge amplification process is then modelled including Gaussian gain fluctuations (in the following also referred to as "noise") and, optionally, a non-linear transfer function. Finally, the resulting charge is digitised with a fixed resolution. Any potential imperfections of the digitisation step are implicitly included in the non-linearities of the amplification step, since they have been found to be tiny for our actual digitiser [16]. Further noise from the read-out electronics is assumed to be negligible in the scope of the detector design studies presented here.

2.1 The case for single-peak resolution

In this section, we will first derive the conditions required to resolve individual peaks in the digitised photomultiplier spectrum. We will then show how the single-peak resolution can be exploited for a reliable estimate of the mean number of Compton electrons per channel, even if the detector behaviour is not perfectly linear.

2.1.1 Requirements for single-peak resolution

Two factors are important to resolve individual Compton electron peaks: the average number of Compton electrons $N_{\text{C.e.}}$ per detector channel, and the number of photoelectrons per electron $p := \frac{N_{p.e.}}{C.e}$. To illustrate this, figure 3 shows a simulation of digitised spectra for $N_{\text{C.e.}} = 5$, with a yield of $p = 7$ and $p = 300$, respectively. Here, a gain g of $4{\cdot}10^5$ with a fixed noise level of $\frac{\Delta g}{g} = 1\,\%$ followed by charge digitisation[5] with a resolution of w_{QDC} =200 fC is assumed as example. For the configuration with $p = 7$, the Poissonian distribution of actual electrons per bunch crossing is smeared into one broad peak. For $p = 300$, however, peaks for the individual actual numbers of Compton electrons $i_{\text{C.e.}}$ can be easily distinguished.

To resolve individual peaks, the separation s between them should be larger than the peak width by a factor k, which can be phrased as a requirement of

$$s > \text{FWHM} = k \cdot \sigma, \tag{3}$$

with σ the width of a Gaussian approximation of an individual peak.

The separation s is determined by p, the photomultiplier gain g and the digitiser resolution w_{QDC} as illustrated in figure 3c:

$$s = p \cdot \frac{g \cdot e}{w_{\text{QDC}}} = p \cdot Q, \tag{4}$$

[4]This is equivalent to a Poissonian (or for large numbers Gaussian) distribution of produced Cherenkov photons and binomial statistics for the detection probability.

[5]In the following we will use the abbreviation QDC (charge sensitive analogue-to-digital converter).

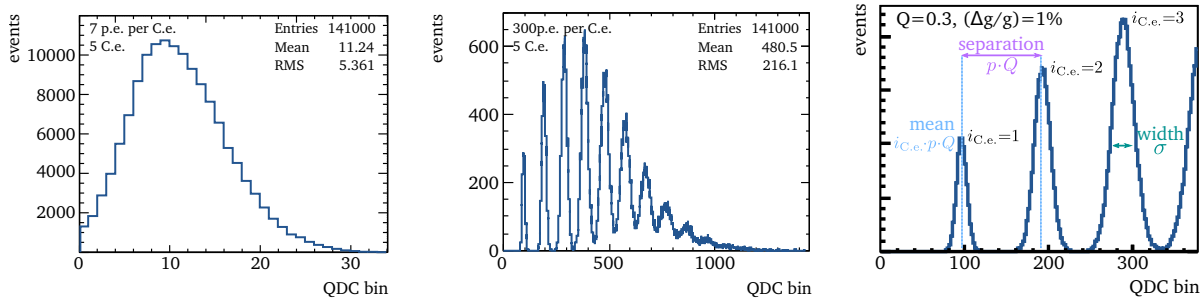

(a) **(b)** **(c)**

Figure 3: Simulated spectra for 5 Compton electrons in the detector with (a) 7 and (b) 300 detected photons per Compton electron. The simulation assumes that the photodetector signal is amplified with a gain of $4 \cdot 10^5$ with a fixed noise level of 1 %, followed by digitisation with a QDC with a resolution of 200 fC. (c) Illustration of peak position, width and separation, for the first three peaks in a simulated QDC spectrum.

where e is the electron charge. The peak width is given by a convolution of the fluctuations in the actual number of photoelectrons per Compton electron around p, the noise $\Delta g/g$ of the photomultiplier, and Q as defined by equation 4, as

$$\sigma = \sqrt{Q^2 \cdot i_{\text{C.e.}} \cdot p + Q^2 i_{\text{C.e.}} \cdot p \cdot (\frac{\Delta g}{g})^2 + \frac{1}{12}}. \tag{5}$$

The first two terms are attributed to the statistics of the photoelectron creation and their amplification, respectively. The term 1/12 accounts for the digitisation error, which is negligible for any of the configurations considered here. To meet the separation requirement given by equation 3 for at least all peaks up to the mean number of Compton electrons $N_{\text{C.e.}}$, a combination with equations 5,4 shows that p needs to fulfil

$$p > \frac{\frac{1}{2} N_{\text{C.e.}} + \sqrt{\frac{1}{4} N_{\text{C.e.}}^2 + \frac{1}{12 \cdot Q^2} \left(\frac{1}{k^2} - (N_{\text{C.e.}} \cdot \frac{\Delta g}{g})^2 \right)}}{\frac{1}{k^2} - (N_{\text{C.e.}} \cdot \frac{\Delta g}{g})^2}. \tag{6}$$

With a choice of $k = 2.35$ for a separation by at least the full width at half max, at least $p > 30$ is required to resolve the case $N_{C.e.} = 5$ for the previous example from figure 3. For the case of $p = 300$ as assumed in figure 3b, up to $N_{C.e.} = 29$ can be resolved.

Obviously, the modelling of the photomultiplier noise is important for a correct estimation of the peak separation capability for a given setup. While the example in figure 3 assumed a constant noise level of 1%, a more realistic approach based on a statistical modelling of the amplification process [17] leads to a dependency of $\frac{\Delta g}{g}$ on the number of photoelectrons which are produced at the cathode. This is taken into account in the simulation studies presented below and results in changes of about 10% in the value of p required to resolve a certain $N_{C.e.}$. Thus equation 6 with a constant noise level remains a useful approximation.

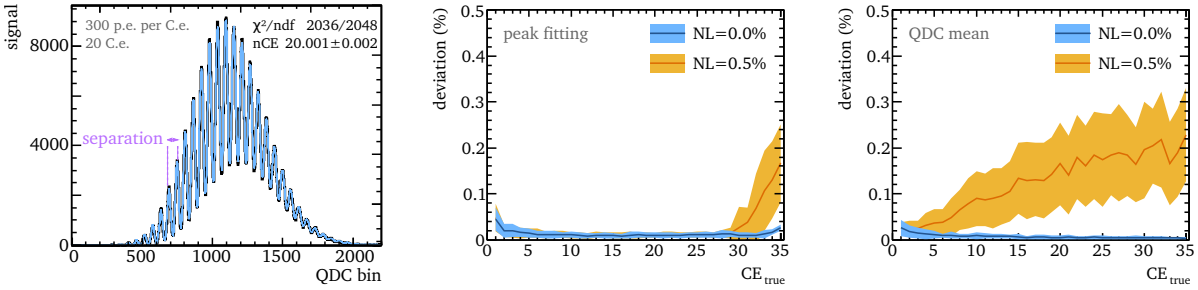

(a) **(b)** **(c)**

Figure 4: (a) QDC spectrum for $N_{\text{C.e.}} = 20$ and $p = 300$ (black histogram) fitted according to equation 7 (blue curve). (b) and (c) show the relative deviation of the measured $N_{\text{C.e.}}$ from its true value when exploiting single peak resolution and when relying on the mean of the QDC spectrum, respectively. The central lines are the mean deviations for 50 simulation runs per value of $N_{\text{C.e.}}$ with $p = 300$, the filled bands represent the RMS around the central value. In case of a perfectly linear detector response, both methods perform equally well (blue). When a photodetector non-linearity of 0.5% is simulated (using non-linearity functions with different randomly selected parameters for each run), the single-peak based reconstruction shows a superior performance (orange).

2.1.2 Reconstruction of $N_{\text{C.e.}}$

The Monte-Carlo simulation described above has been employed to obtain QDC spectra for various conditions. As example, the histogram in figure 4a shows the predicted QDC spectrum for $N_{\text{C.e.}} = 20$ assuming $p = 300$, $g = 2.4 \cdot 10^5$ with detailed modelling of the noise, perfect linearity and $w_{\text{QDC}} = 200\,\text{fC}$. There are two possibilities to reconstruct the average number of Compton electrons from this spectrum: either by taking the mean (or maximum) of the whole distribution as in the case with no single-peak resolution, or by extracting $N_{\text{C.e.}}$ from a fit to the detailed shape of the spectrum.

A suitable fit function is the sum of Gaussians with mean $q_{2\cdot i_{\text{peak}}}$ and width $q_{2\cdot i_{\text{peak}}+1}$, where each Gaussian describes one of n_{peaks} peaks in the spectrum. Since the number of electrons in a channel is expected to follow a Poissonian distribution, the height of the peaks is set to the expectation for i_{peak} electrons from a Poissonian distribution of $N_{\text{C.e.}}$ electrons and scaled to the number of events N_{events} in the spectrum:

$$f(x_{QDC}) = N_{events} \cdot \sum_{i_{\text{peak}}=0}^{n_{\text{peaks}}} \text{Pois}(i_{\text{peak}}, N_{\text{C.e.}}) \cdot \text{Gaus}(x_{QDC}, q_{2\cdot i_{\text{peak}}}, q_{2\cdot i_{\text{peak}}+1}). \tag{7}$$

The free parameters of the fit are the mean and width of all n_{peaks} peaks and the central value $N_{\text{C.e.}}$ of the Poissonian. While studying the distance between the mean values of the individual peaks gives access to the gain linearity, the central value $N_{\text{C.e.}}$ of the Poissonian is the parameter of interest for the polarisation measurement. An example for a fit of equation 7 to a spectrum simulated with $N_{\text{C.e.}} = 20$ is shown in figure 4a for 10^7 accumulated individual measurements.

The number of parameters to be fitted grows with the number of electrons per detector channel. For $N_{\text{C.e.}} = 20$, peaks up to $i_{\text{C.e.}} \approx 40$ need to be described in the QDC spectrum and consequently a fit function with ≈ 80 parameters is required. For such a large number of free parameters, a careful choice of start values for the fit is essential. Since the distance between neighbouring peaks is constant for a perfectly linear photomultiplier and changes only gradually for non-linear gain, an initial estimate for s can be obtained from the discrete Fourier transform of the spectrum. From the separation, start values for the Gaussian parameters can be determined by calculating the expected mean and width. Since s corresponds to the scale factor between initial Compton electrons and QDC bins, a start value for $N_{\text{C.e.}}$ can be obtained by fitting a Poissonian $P(x')$ with $x' = \frac{x_{QDC}}{s}$ to the spectrum.

Figure 4b shows the relative deviation of the fit result for $N_{\text{C.e.}}$ from its true value for up to $N_{\text{C.e.}} = 35$ in case of a perfectly linear response (blue) and in the presence of a photodetector non-linearity of 0.5 %.

Up to $\sim$25 Compton electrons, the added non-linearity has little effect. For larger number of electrons, the description of the spectrum by the fit start values does not model the spectrum shape sufficiently well anymore and the fit results starts to degrade. For comparison, figure 4c shows how much a photodetector non-linearity of 0.5 % affects the conventional method using the mean of the QDC spectrum, which is the only method for the calculation of the polarisation asymmetry when no single-peak resolution is possible.

2.2 Application to polarisation measurements at the ILC

The results in figure 4 where based on accumulating 10^7 individual measurements. With the baseline beam parameters of 1312 bunches per bunch train at 5 Hz bunch crossing rate, $3.936 \cdot 10^6$ measurements could be collected in 10 minutes, providing a large enough data sample so that the fit performance is not limited by statistics. Since the non-linearity is not expected to change rapidly, the actual polarisation measurement can be done on much smaller datasets, with a determination of the peak positions from the data taken in the previous 10 minutes or, in an offline analysis, with a moving average over data taken before and after the individual short-time dataset.

To evaluate the benefits of the fit procedure described above for polarisation measurements at the ILC, a detector array of 60 channels with a width of 3 mm and 0.33 mm inter-channel spacing was simulated. The fast Linear Collider Polarimeter Simulation `LCPolMC` is used [8, 13] to generate Compton events and subsequently track the Compton electrons through the polarimeter chicane to the detector. The beam and laser parameters used for the simulation are chosen according to the expectations at the polarimeter locations for the ILC TDR beam parameters [2]. Figure 5a shows the resulting number of Compton electrons per channel. It is below $N_{\text{C.e.}} = 30$ for all channels, and consequently the requirement for single-peak resolution given by equation 6 is fulfilled.

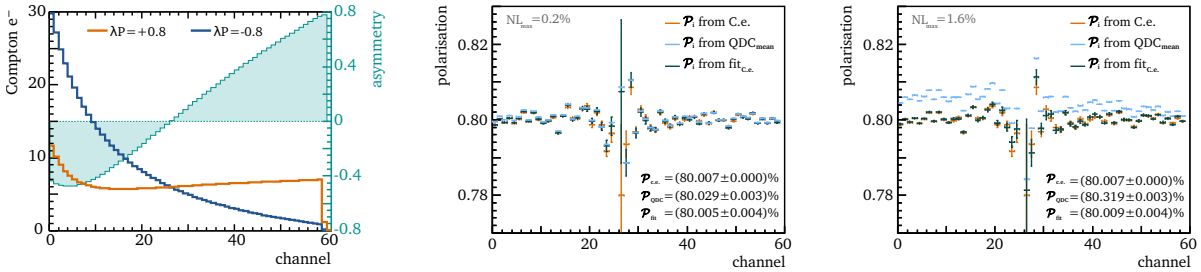

(a) **(b)** **(c)**

Figure 5: (a) Mean number of Compton electrons per detector channel for $\lambda\mathcal{P} = \pm 80\%$ and the corresponding asymmetry assuming 60 channels. (b) and (c) Polarisation calculated for each detector channel i for a simulation of 80% polarisation with 0.2% and 1.6% photodetector non-linearity, respectively. The orange markers show the polarisation $\mathcal{P}_{\mathrm{C.e.,i}}$ calculated from the primary Compton electrons, the blue markers the calculation $\mathcal{P}_{\mathrm{QDC,i}}$ from the mean of the QDC spectrum, and the dark green markers the results $\mathcal{P}_{\mathrm{fit,i}}$ for the number of Compton electrons determined from the fit to the QDC spectra.

2.2.1 Robustness against non-linear detector response

Based on figure 5a, the same simulation chain as before is applied to all channels for both laser helicities and the average number of Compton electrons per channel is extracted both from single-peak fitting and from the mean of the QDC spectrum. The polarisation is then reconstructed as described in section 1.

Figure 5b compares the polarisation measurements obtained via the two reconstruction methods in case of a rather small non-linearity of 0.2% with the ideal result obtained directly from the true Compton electron spectrum. While the results from the three different methods exhibit no striking difference in this case, a larger non-linearity of 1.6 % as shown in figure 5c distorts the QDC mean and therefore the measured polarisation significantly, with a relative deviation of 0.39 %, while the polarisation calculated from the fit results appears to be unaffected, with a deviation of 0.01 %.

For a more systematic survey of the impact of non-linearities, the same procedure as for figure 5b was repeated for non-linearities from 0 % to 4 % in 0.2 % steps. For each step, random parameters for 100 different functions for the photomultiplier non-linearity were picked and used for the spectrum generation. The mean and RMS of the deviation between the polarisation determined from the mean of the generated QDC with respect to the result for the primary electron calculation is shown in figure 6a. The error budget for the detector linearity contribution to the polarisation measurement is 0.1 % (see table 1). The method using the mean of the QDC surpasses the allocated limit for non-linearities $\gtrsim 0.4\,\%$. The results for the polarisation calculation from the fitted number of Compton electrons is shown in figure 6b. Fitting the QDC spectra instead of using the mean can compensate the photodetector non-linearity well enough to stay within the error budget for non-linearities up to $\sim 2.2\,\%$.

This can be further improved by introducing a second step in the calculation of the polarisation to eliminate the contribution from outlier channels with poor fit performance.

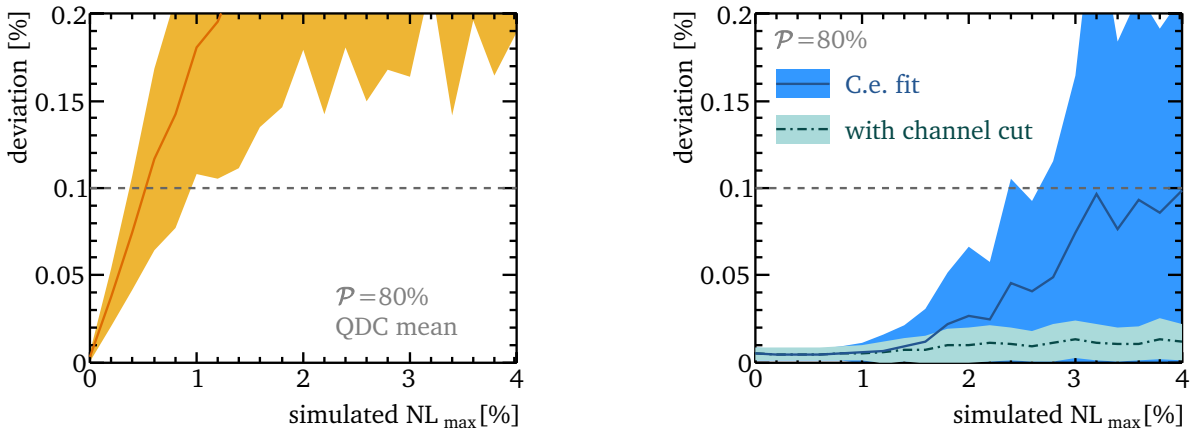

Figure 6: Deviation between the result from the polarisation $\mathcal{P}_{\text{C.e.}}$ calculated from the primary Compton electrons and (a) the polarisation $\mathcal{P}_{\text{QDC}}$ determined from the mean of the QDC spectrum, and (b) the polarisation $\mathcal{P}_{\text{fit}}$ calculated with the number of Compton electrons determined from the fit of the QDC spectra, using all detector channels (blue, solid line) or only those channels i whose polarisations $\mathcal{P}_{\text{fit,i}}$ agree within $\pm 1\% \cdot \mathcal{P}_{\text{fit}}$ with the polarisation calculated from all channels (green, dash-dotted line).

A rough first approach to demonstrate this is a recalculation of the polarisation using only the channels which agree within $\pm 1\,\% \cdot \mathcal{P}_{\text{fit}}$ with the polarisation calculated from all channels. The fraction of channels consequently used in the calculation is larger than 90 %. Using less channels will decrease the statistical precision slightly. However, the benefits of this approach in dealing with larger detector non-linearities, compared to the use of all channels, are clearly visible in figure 6, where the deviation between the polarisation thus obtained with respect to the result for the primary Compton electrons is shown in green. Even for photodetector non-linearities of 4 %, this deviation is below 0.03 %, i.e. well within the error budget of 0.1 %, which would be a contribution towards reducing the overall systematic uncertainty on the polarisation measurement. For the method using the QDC mean, such an approach would not lead to such improvements, since all channels are systematically affected by the non-linearity, as one can see when looking at the example in figure 5c.

2.2.2 Detector alignment

Next to non-linearities, the detector alignment with respect to the Compton electron fan is the other large contribution to systematic uncertainties on the polarisation measurements that should be taken into account in the design of the polarimeter detectors, c.f. table 1. The largest contribution originates from the alignment in the plane of the magnetic chicane, since it directly affects the analysing power predicted for each channel.

Rotations of the detector in the deflection plane of the chicane (i.e. in the horizontal plane, staying with example of the upstream polarimeter) affect the path of the electrons

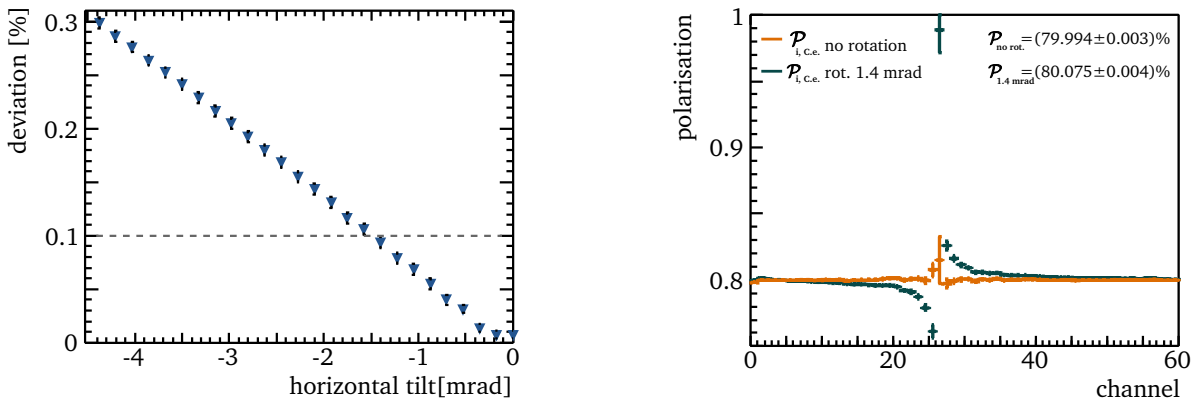

Figure 7: (a) Deviation of the polarisation obtainable from the primary Compton electrons in dependence of detector rotation in the horizontal plane for a simulation of 80 % polarisation, and (b) the polarisation calculated for each detector channel i without detector misalignments and in case of a 1.4 mrad tilt in the horizontal plane.

through the channels. The amount of Cherenkov light per electron and its propagation to the photodetector could be altered, thus changing p. This effect has to be found negligible for all simulated angles up to 5°. More importantly, such horizontal tilts can introduce cross-talk if a Compton electron passes through more than one channel. Figure 7a shows the impact on the polarisation: tilts of the detector in the horizontal plane result in deviations of 0.07 %/mrad. For the ILC polarimeters, a tilt alignment of 1 mrad or better is considered feasible, thus the corresponding systematic uncertainty is within the allocated error budget. Horizontal rotations of the detector have the strongest impact on the channels with the smallest asymmetries near the zero-crossing of the asymmetry, as can be seen in figure 7b. This characteristic pattern can be resolved with high granularity as in case of the 60 channels considered here. Consequently, the systematic uncertainties could be further reduced by identifying the presence of misalignments and correcting for them or excluding the most strongly affected channels.

Misalignments of the detector position in the horizontal direction can be controlled by monitoring the fraction of Compton electrons in the detector channel at the Compton edge. Figure 8a shows how the fraction of Compton electrons in the detector channel containing the Compton edge over the total number of detected electrons changes as a function of a horizontal offset of the detector.

$$y = \frac{N_{\text{C.e}}(i_{\text{edge}})}{\sum_{i=1}^{N_{\text{chan}}} N_{\text{C.e}}(i)}. \tag{8}$$

Averaging over the measurements with both laser helicities eliminates any dependence on the polarisation, as can be seen in figure 8a. A fit of a linear function to this ratio yields a slope m of $-0.343\,\frac{\%}{\text{mm}}$. It should be noted that the expected number of Compton electrons hitting the front face of each detector channel for a given offset is independent from intrinsic detector uncertainties and thus the precision of m is only limited by the

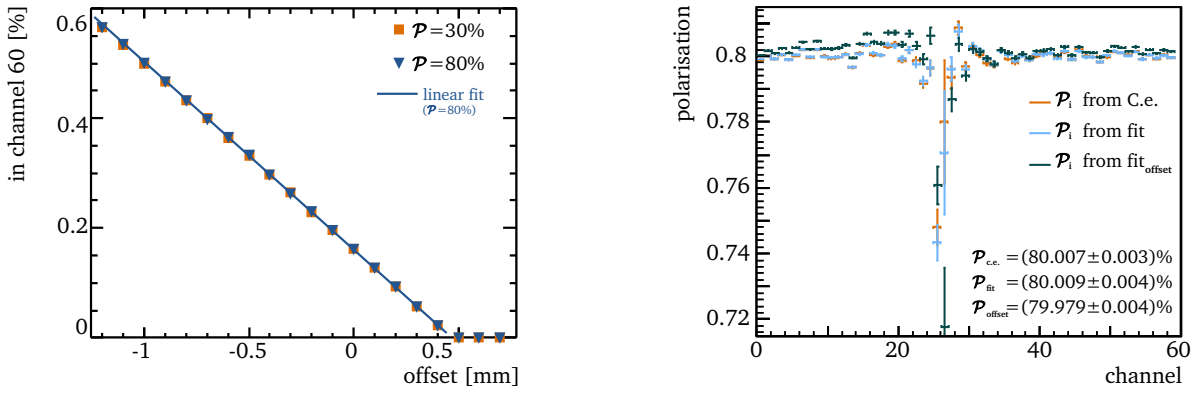

(a) **(b)**

Figure 8: (a) Fraction of Compton electrons expected in the detector channel containing the Compton edge as a function of a horizontal offset for $\mathcal{P} = 30\,\%$ and $80\,\%$ polarisation, averaged over the measurements with both laser helicities. A first order polynomial has been fitted to the $80\,\%$ case. (b) Polarisation $\mathcal{P}_{\text{offset,i}}$ calculated for each detector channel i for a simulation of $80\,\%$ polarisation with a horizontal misalignment of $\sim 50\,\mu$m (dark green). For comparison, the blue (orange) markers show the polarisation $\mathcal{P}_{\text{fit,i}}$ ($\mathcal{P}_{\text{C.e.,i}}$) obtained without misalignment from the fit to the QDC spectra (the primary Compton electrons).

knowledge of the field of the chicane magnets, which is expected to be much better than the detector-beamline alignment.

In case of single-peak resolution, $\Delta N_{\text{C.e}}(i) = 0.1\,\%$ is estimated for the determination of the Compton electron number per channel based on the performance shown in figure 4b, which holds even in case of a not perfectly linear detector response [6]. By propagating the assumed uncertainty for each channel to the ratio y, $\Delta y = 7.9 \cdot 10^{-4}$ % is obtained, which translates into a horizontal alignment precision of $\Delta x = |\Delta y / m| = 2.3\,\mu$m.

Such an alignment is sufficient to meet the requirements on the contributions to the systematic uncertainty of the polarisation measurement from the detector alignment. Figure 8b shows the impact that of horizontal misalignment of $50\,\mu$m in a simulated polarisation measurement. The deviation of $\Delta\mathcal{P}/\mathcal{P} = 0.03\,\%$ caused by the offset is well within the allocated error budget. Thus fitting the single-electron-peak spectra is also a promising approach towards meeting the requirements for the detector alignment.

3 Design of a quartz Cherenkov detector

For the baseline gas Cherenkov detector with 1 cm wide channels, the mean number of Compton electrons per channel reaches up to $N_{\text{C.e.}} \simeq 100$, while the average yield of photoelectrons per Compton electron is $p = 6.5$ [9]. This configuration is far from

[6] The same method can also be applied when relying on the mean of QDC spectrum only. In that case, however, the precision degrades significantly in case of non-linearities, c.f. figure 4c.

fulfilling equation 6. In order to develop a Cherenkov detector suitable to achieve single-peak resolution, there are two possibilities: The number of Compton electrons per channel can be reduced by a factor 2-3 by building smaller channels for the polarimeter. In addition, it is mandatory to increase the number of photoelectrons per Compton electron substantially. As an approach to achieve the latter, the use of quartz as Cherenkov material is considered. The higher refractive index compared to Cherenkov gases results in a much higher light yield, as described by the Frank-Tamm formula [18]. Compared to e.g. perfluorobutane gas, the use of quartz would translate into an approximately 200 times higher intensity of the emitted Cherenkov light for relativistic particles. However, this will be somewhat mitigated by other effects, such as increased absorption as the produced light travels to the photodetector. In this section, we discuss a simulation study of these effects and derive a suitable design for a prototype detector.

3.1 Geant4 simulation

To study the feasibility of a quartz detector for ILC polarimetry and investigate different design options, as well as for comparison to data from a prototype detector, a detailed simulation of the detector concept based on GEANT4 [19] has been developed. The simulated geometry is depicted in figure 9. The main elements of the simulated setup are quartz blocks surrounded by a thin layer of air and/or aluminium foil, the entrance window and photocathode of a photomultiplier tube (PMT) and a layer of optical grease between the quartz block and the PMT window. To increase the space available for the photodetectors and their readout, every other quartz block is flipped with respect to its neighbours.

To produce Cherenkov light, electrons are shot through the quartz. For the Cherenkov photons, all relevant processes are simulated, in particular absorption according to the absorption length of the relevant material, Rayleigh scattering, and boundary processes at the surface between two different media. For the detector material, the optical properties of Spectrosil® 2000 [20] have been implemented, and for the optical grease the properties of Cargille fused silica matching liquid code 06350 and 50350 [21]. To describe the behaviour of the photons at boundaries between materials, the UNIFIED model [22] of GEANT4 is used.

Various geometrical properties were varied to study their impact on the light yield:

- A larger channel width L_x reduces the number of reflections at the channel walls a photon undergoes before detection, which increases the probability to arrive at the photodetector.
- A larger channel height L_y increases the path length of the electron crossing the quartz channel and consequently the amount of Cherenkov light produced. Additionally, as in the case of larger width, the number of reflections is reduced. Both effects result in an enhanced photon yield.
- A shorter channel length L_z reduces the distance the photons have to travel before detection, which increases the light yield by causing less photons to be absorbed inside the quartz.

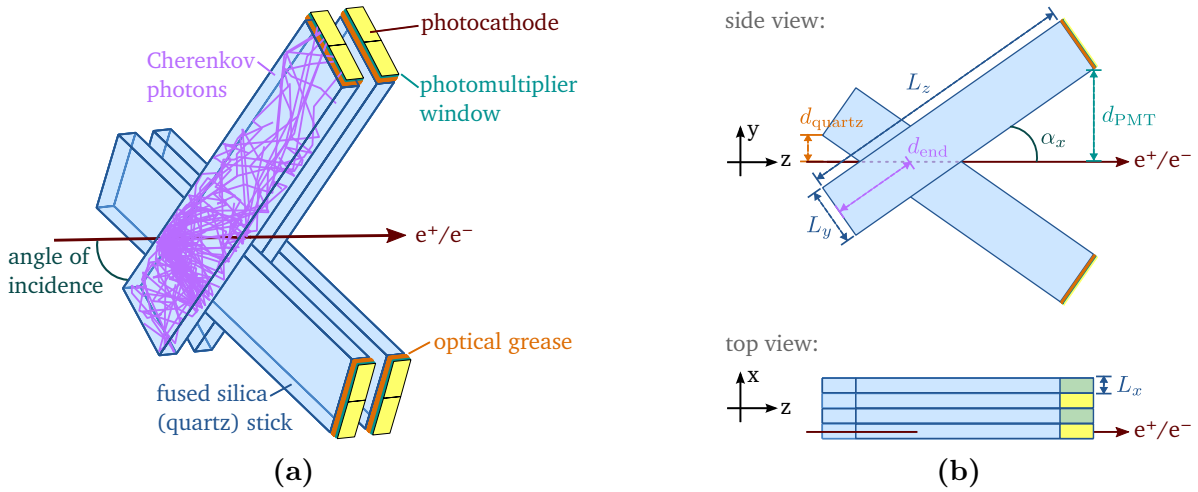

Figure 9: Sketch of the simulated geometry. The left side (a) shows some components of the simulation, in addition demonstrating the added space for electronics due to the rotation of every second quartz block. For a better overview, on the right side (b) the same geometry is depicted in side- and top-view, along with the geometrical parameters varied in the design studies: the channel dimensions width L_x, height L_y, length L_z; the incidence angle α_x; as well as the space between quartz and electrons d_{quartz}, between electrons and PMT d_{PMT}, and the distance between the end of the channel and the point where the electron crosses the detector axis d_{end}.

- The incidence angle α_x of the electron into the quartz channel also changes the path length of the electron crossing the quartz channel for light production, with a higher light yield for small angles. Another, though less pronounced, impact on the number of photons is due to the fact that for angles close to the Cherenkov angle, a larger fraction of the photons can reach the detector without being reflected on the narrow side faces. The spatial distribution of the light on the photodetector surface is the most uniform under such angles, whereas for smaller or larger angles the intensity distribution is less homogeneous, as illustrated in figure 10. This effect could possibly aid in the angular alignment of the detector if a photodetector with multiple anodes per quartz channel was used.

When combining the parameters listed above to chose a suitable detector geometry, some considerations have to be taken into account in addition to the light yield. Small channel width lead to less Compton electrons per detector channel and therefore aid in fulfilling the condition for reaching single peak resolution. Another consideration is that long, narrow channels and large angles move the photodetector further from the Compton electrons to protect them from contact with high energetic particles. To take this into account, the channel height and the electron entrance point were varied along with the length, such that the space between the lower end of the quartz and the electron plane stayed constant at $d_{\text{quartz}} = 10.0\,\text{mm}$ and the shortest distance between the electrons and the photomultiplier was $d_{\text{PMT}} = 30.0\,\text{mm}$. This translates into a channel height L_y of

$$L_y = \frac{2 \cdot L_z \cdot \sin(\alpha_x) - d_{\text{quartz}} - d_{\text{PMT}}}{2 \cdot \cos(\alpha_x)} \tag{9}$$

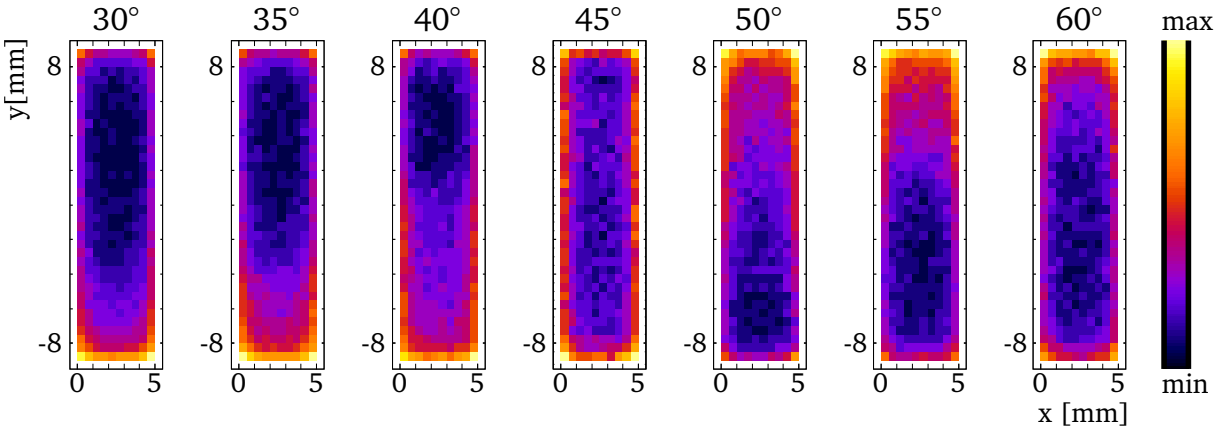

Figure 10: Light distribution on the photocathode for different incidence angles of the electron. The position on the photocathode surface is coloured according to the relative light concentration: the regions with most light for each angle are shown in yellow, with a colour gradient to the regions with the least light in dark blue.

and a distance d_{end} between the end of the detector channel and the electron crossing of the detector axis of

$$d_{\text{end}} = \frac{d_{\text{quartz}} + L_y \cdot \cos(\alpha_x)}{\sin(\alpha_x)} \tag{10}$$

for each simulated channel length L_z and incidence angle α_x. The results for channel lengths in the range 50 mm – 300 mm and angles in the range 30°– 60° are displayed in figure 11. In this range of parameters, the best photon yield of ∼3000 photons was achieved for $\alpha_x = 60°$ and $L_z = 160.0$ mm, which allows a channel height of $L_y = 197.2$ mm while keeping the chosen safety margin between incoming electrons and readout electronics. A mechanical setup with such nearly square-shaped channels rather than elongated ones might pose some challenges, e.g. covering the readout face of high but narrow with conventional PMTs does not seem reasonable with standard photomultiplier geometries. However figure 11 shows that there is a large variety of configurations with less extreme aspect ratios which still offer an impressive light yield in the order of ∼1500 to ∼2000 photons and which would be more straightforward to implement.

For the construction of the prototype detector (section 3.2), smaller dimensions of $L_y = 18.0$ mm and $L_z = 100.0$ mm were chosen, despite the prediction of less (∼600) photon hits. This choice was partly made to match the dimensions of the available photodetectors, but also to maintain the angular flexibility to scan the full range from 30°– 60° to confirm the incidence angle's effect on the light distributions.

The photon hits given above are the number of photons that reach the photodetector surface. Most common photodetectors have a detection efficiency well below 100 %. A more realistic estimate of the photon yield which could be achieved will therefore have to take the characteristics of the photodetector into account to evaluate the number of detected photons. Figure 12a shows the quantum efficiencies of two PMTs with good sensitivity in the UV range.

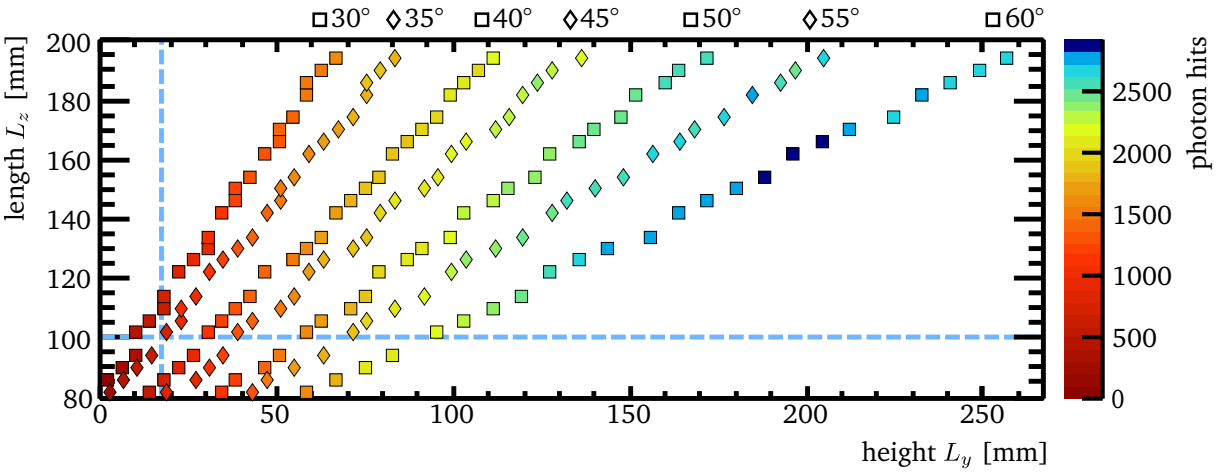

Figure 11: Photon hits for different quartz lengths, heights and angles relative to the electron chosen such that conditions 9 and 10 are fulfilled. The dashed blue lines indicate the length and height used for the prototype detector.

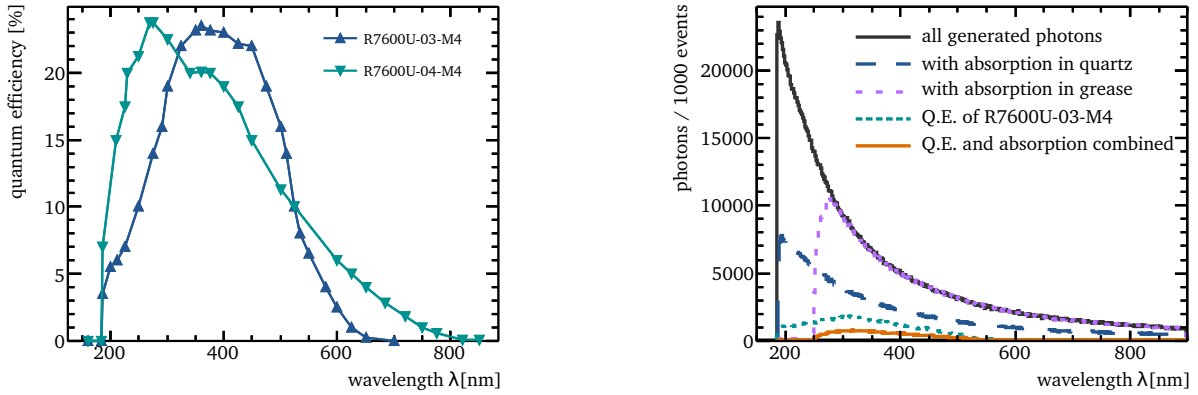

(a) **(b)**

Figure 12: Effect of photomultiplier choice: the left plot (a) shows the quantum efficiencies of two UV sensitive PMTs [23]. On the right (b), the wavelength spectrum of the Cherenkov photons and the effects of absorption inside the detector and the different quantum efficiencies is shown.

The amount of measurable light can be further influenced by the choice of the other materials used in the detector, such as the type of optical grease or the surface finish of the quartz bars. The impact that the choice of photodetector and materials has on the amount of measurable light is illustrated by figure 12b. Despite the fact that layer of grease is only 1 mm thick, the UV component of the Cherenkov light is severely affected by its short absorption length. This clearly indicates that the choice of a suitable optical grease to couple the photodetectors to the quartz is also of great importance. The application of another optical grease with lower absorption in the UV range would allow to increase the amount of measurable light for a chosen geometry. To a smaller extent, further improvements could be achieved by polishing the quartz surface. Table 2 lists the predicted light yield for both the geometry with maximum predicted light yield from figure 11 as well as for the prototype discussed section 3.2 (with a size of 5 mm × 18 mm

simulated geometry:	optimised		prototype	
	ground	polished	ground	polished
photon hits	3344 ± 58	3876 ± 62	576 ± 24	651 ± 26
detected photons	322 ± 18	373 ± 19	57 ± 7	60 ± 8

Table 2: Light yields (with statistical errors) for an optimised geometry and the prototype detector geometry. The values for "photon hits" refer to the number of photons reaching the readout at the end of the channel per incident electron, while "detected photons" are those remaining after absorption in Cargille 50350 optical grease and application of the quantum efficiency of a Hamamatsu R7600U-03 PMT.

$\times$ 100 mm and for an incidence angle of $\alpha_x = 45°$). Despite the fact that only $\mathcal{O}(10\,\%)$ of the photons are detected with the material choices considered in these first simulation studies, the predicted yield of 60 – 300 detected photons per incident electron are promising for achieving a single Compton electron resolution as discussed in section 2. For the prototype geometry along with a PMT gain of $g = 4 \cdot 10^5$ and a digitiser with a resolution of 200 fC, this would correspond to an allowed range of up to $N_{\text{C.e.}} = 10$ electrons per channel, while a light yield of 200 – 300 as predicted for other geometries would allow $N_{\text{C.e.}}$ =28 – 42 electrons per channel.

3.2 Construction of the prototype

The simulation studies indicate that the desired photon yield can be reached. To verify the simulation's predictions, a prototype detector with adjustable incidence angle was built and operated at the DESY II testbeam.

The prototype detector consists of four quartz bars, with every second quartz block flipped with respect to its neighbour, as described in section 3.1. The synthetic fused silica brand Spectrosil® 2000 [20] was selected as the most suitable material, based on the high radiation tolerance compared to other natural or synthetic fused silica brands [24], the low number of optical impurities and the high transmission in the UV range. The dimensions of each quartz block were chosen to be 5 mm $\times$ 18 mm $\times$ 100 mm, which is a suitable compromise between a high light yield and off-the-shelf photodetector geometries. Each quartz block was wrapped in aluminium foil as shown in figure 13a.

The photodetectors for the prototype detector were chosen according to two main criteria: high quantum efficiency at short wavelength, where the Cherenkov light intensity is the highest, and the dimensions of the sensitive area. Square photomultipliers with an active area of 18 mm $\times$ 18 mm, with a four-anode readout (Hamamatsu R7600U-03-M4 and R7600U-04-M4) were employed to read out the two quartz blocks pointing into the same direction, with two anodes covering one quartz block as illustrated in figure 13b. This layout allows to have the four detector channels directly side-by-side. Figure 13c shows two quartz blocks and one of the PMTs compared to a 2-Euro coin.

To limit the occurrence of total reflection at the boundary between quartz bar and PMT window, they need to be coupled with optical grease. For the testbeam campaign, Cargille 06350 was used.

The mechanical setup to hold the quartz bars and photomultipliers in place with adjustable angle between them is shown in figure 14a. The angle between the upper and lower channels can be controlled by the movement of a stepping motor with a base step angle of 0.9°, which is transformed to 0.5° steps by a dedicated gear mechanism contained in the mechanical setup.

4 Single electron measurements at the DESY testbeam

The quartz prototype detector was characterised with single electrons at the DESY testbeam [25]. The electrons are produced by inserting a metal conversion target into a bremsstrahlung beam from the DESY II synchrotron. As a converter target for the generation of the electrons, a copper foil of 5 mm thickness was chosen. With a dipole magnet and a collimator electrons with an energy of 3.75 GeV were selected to achieve a high rate for the data taking. In combination with an area collimator with aperture of 5×5 mm located 5 m upstream of the prototype detector, this resulted in single electrons reaching the prototype detector with a frequency of ≈1 kHz – 2 kHz.

The quartz detector was placed inside an aluminium box with foam rubber seals to shield it from external light and placed on a base plate movable by two linear precision translation stages, as shown in figure 14b.

The main components of the setup and the readout chain during the testbeam campaign are sketched in figure 15a: The photomultipliers are operated with a supply voltage of 900 V, leading to amplification with a gain of $\sim 1.5 \cdot 10^6$ (c.f. section 4.5). The charge signals of the photomultipliers are read out with a 12-bit charge-sensitive analogue-to-digital converter (QDC) which offers two resolutions, 25 fC and 200 fC. The digitisation

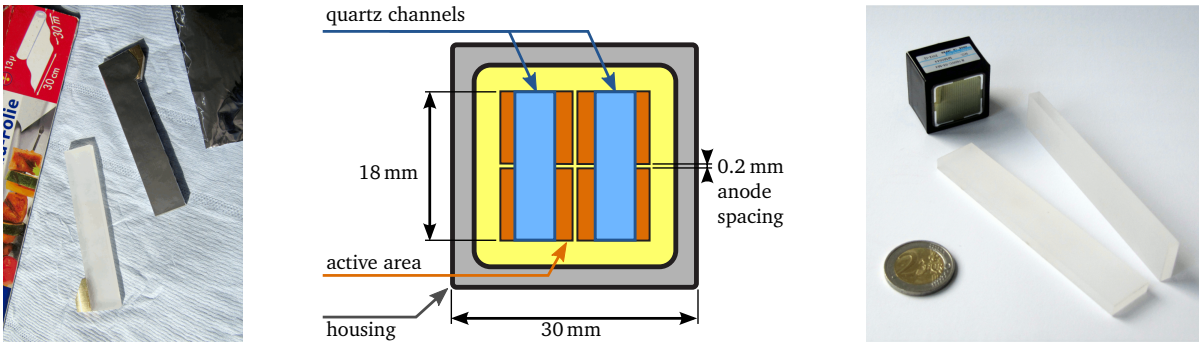

(a) **(b)** **(c)**

Figure 13: (a) Quartz blocks with the coupling piece used to attach them to the mechanical holder, in the process of being wrapped in aluminium foil. (b) Sketch to illustrate how one photomultiplier with four readout-anodes can be positioned to provide two measurements for two quartz channels each. (c) Quartz blocks and a photomultiplier with a coin for size comparison.

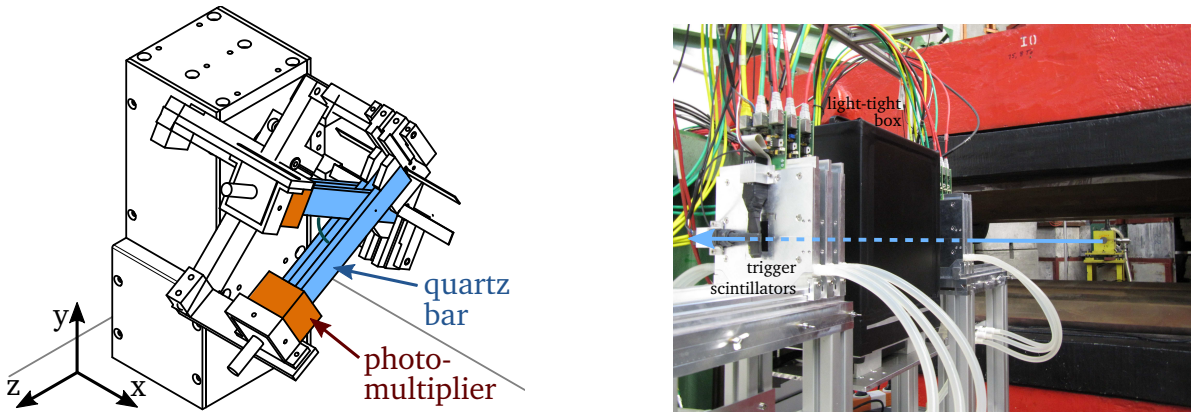

(a) (b)

Figure 14: In the technical drawing (a), the positioning of the four quartz blocks and two photomultipliers used in the prototype setup are marked. On the photo of the testbeam setup (b) a sketch of the beam path is overlaid on a close-up of the light-tight box with the detector inside on the x-y-table and two of the trigger scintillators.

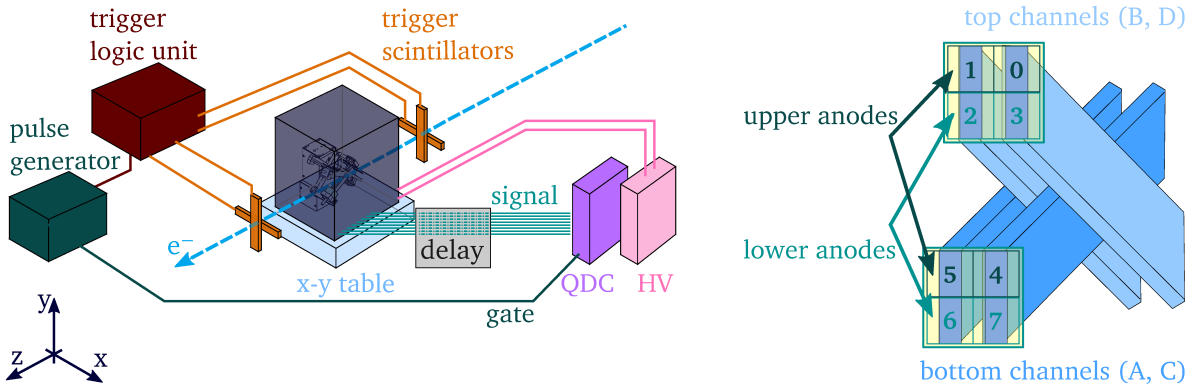

(a) (b)

Figure 15: (a) Experimental setup at the testbeam. The main components of the setup and the path of the readout signal path are sketched. (b) Channel names and anode numbering used for the description of the testbeam data.

length and cycle are steered by an external gate. To trigger on beam electrons, the generation of the gate signal was started in case of a four-fold coincidence between two trigger scintillators before and after the detector, respectively. A total number of eight QDC channels was used to digitise the signal from the two four-anode photomultipliers. The conventions for channel naming and anode numbering are illustrated in figure 15b. An example for the QDC signal recorded for a PMT anode is shown in 16a.

As a first step the detector response and alignment of the testbeam setup were studied, which consequently allowed to compare the measured data to simulation and evaluate the light yield.

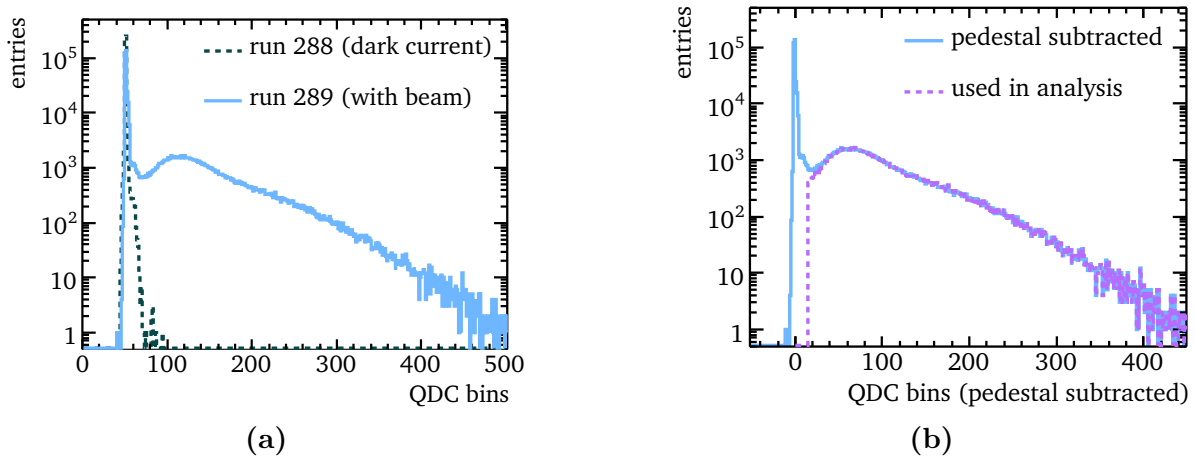

Figure 16: Pedestal correction. (a) An example for an uncorrected QDC spectrum is shown in light blue, recorded in anode 5 with the beam centred on channel A and a beam incidence angle of 45°. A dark current spectrum for the same anode is drawn in dark green (dashed line). (b) The same QDC spectrum with shifted x-axis to correct for the pedestal contribution. The light blue histogram contains all events, while the violet histogram (dashed line) is made up of only the events used in the analysis, i.e. events in which both anodes of a channel see a signal of at least 15 QDC bins above the pedestal.

4.1 Detector response

The spectrum of each photomultiplier anode contains events in which the data acquisition was triggered, but no electron entered the respective channel. Therefore, in addition to the Cherenkov signal another peak is present at the low edge of the spectrum, caused by the QDC pedestal and broadened by dark current from the photomultipliers.

To exclude events in the analysis of a detector channel where that channel was not hit by the electron beam, a cut threshold was defined based on dedicated dark current measurements (i.e. runs without beam) taken over the course of the testbeam period. It was found that applying a threshold of 15 QDC bins above the QDC pedestal position eliminates at least 99.7 % of the events in any dark current spectrum. For the analysis of the data, only events where selected in which both anodes of a channel yield a signal of at least 15 QDC bins above the mean of their respective pedestal. The part of the spectrum used in the analysis, compared to the spectrum before any cuts, is depicted in figure 16b.

Figure 17 shows the signal of a single anode in both data and simulation. To convert the number of detected photons in the simulation to QDC bins, a gain of $1.3 \cdot 10^6$ (c.f. section 4.5) and the same digitiser resolution as in the data were assumed.
In the data, the QDC signal has a noticeable tail to higher charges. The most likely explanation is the presence of secondary electrons in addition to the main beam electron, which would produce some additional light when they hit one of the quartz channels. It is currently not clear where these stem from. The wall thickness of the light-tight box surrounding the detector is only 4 mm, which does not account for enough shower electrons to explain the amount of additional light observed. Other possible contributions

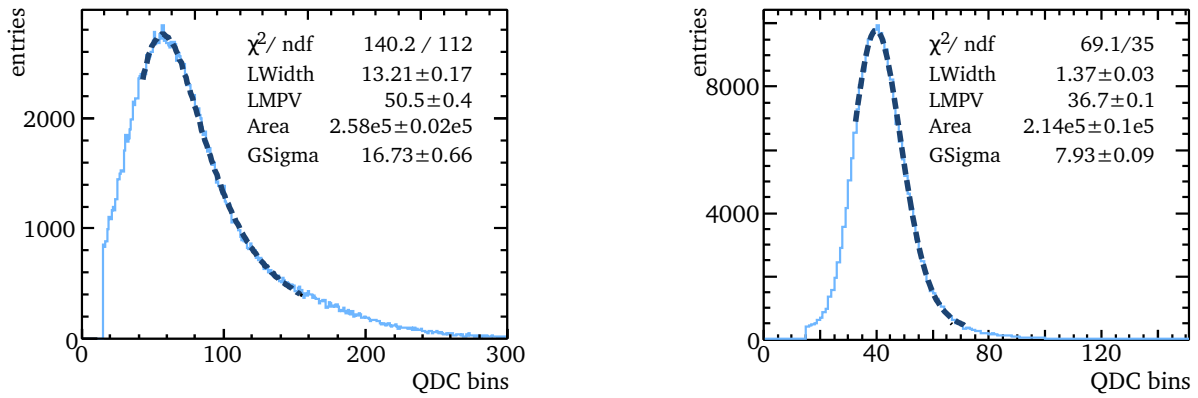

Figure 17: Fit of a Landau function convoluted with a Gaussian to the signal for (a) anode 2 in a data taking with the beam centred on channel B, under an incidence angle of 30° and (b) the corresponding simulation. The cut-off at low QDC bins is due to the pedestal subtraction cut.

along the beam line have not been investigated so far.
To account for the tail in the distribution, the QDC signals were fitted with a fit function consisting of a Landau function convoluted with a Gaussian. The free parameters of the function are the width and most probable value (MPV) of the Landau function, the sigma of the convoluted Gaussian and a normalisation constant for the peak area. Whenever the testbeam data is compared with the simulation, the same fit is applied to the simulation. For the simulation, the width of the Gaussian is dominant, and the relation between MPV and the Gaussian width is consistent with the expectations from the statistical modelling used for the fast simulation introduced in section 2. In the data, the Gaussian width is roughly twice as large as one would expect from noise in the amplification process alone. Since this broadening was not observed in a separate setup in the laboratory, it is attributed to the experimental environment at the testbeam, such as the long signal cables. The width of the Landau part of the fit function required to describe the large tails in the data is comparable to the Gaussian width.

The most probable value of the fitted Landau function was used as a measure for the amount of light in a channel, while the area parameter is related to the number of times a channel was hit by the beam. To illustrate the stability of the detector response and the fit procedure's outcome, figure 18a shows the fitted most probable value for both anodes of a channel for a number of data taking runs at identical beam position over a period of several hours.

4.2 Horizontal alignment and beam profile

To determine how well the prototype detector can be aligned from data alone, the detector position was scanned by varying the position of the movable table in x-direction in 1 mm steps. Studying the observed number of events in each detector channel for the different x-positions allows to determine the position of the channel with respect to the beam, as

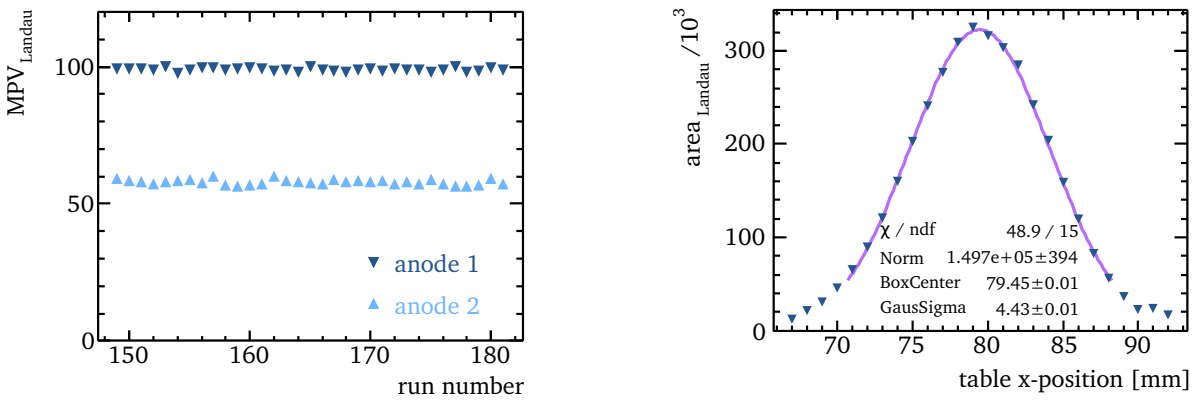

Figure 18: (a) Fit results anodes 1 and 2 for 32 for consecutive measurement runs taken over a period of 11 hours (beam on channel B, under an angle of 30°). The observed light yield stays constant. (b) Landau area of anode 1 observed at different x-positions of the detector, fitted with a box function convoluted with a Gaussian (as in equation 11).

well as derive information on the size and shape of the beam spot. For a pointlike beam and perfect alignment, the channel response would be expected to have a "box-like" shape, whereas a finite beam-size and tilts around the vertical axis will smear out the edges of this step response function. To determine the channel centres, the measurements for each anode were fitted with a box function convoluted with a Gaussian. The box function is 1 for all x within $\pm 2.5\,\mathrm{mm}$ of its central value, to describe the prototype channel width of 5 mm, and the Gaussian is used to account for the smearing. The convolution is implemented as sum within four sigma of the Gaussian, i.e.

$$f(x) = p_0 \cdot \sum_{\tau=p_1-4\cdot p_2}^{p_1+4\cdot p_2} \mathrm{box}(\tau, p_1) \cdot \frac{1}{p_2\sqrt{2\pi}} e^{-(x-\tau)^2/2\cdot p_2^2}, \tag{11}$$

where the free parameters are a normalisation factor p_0, the centre position p_1 of the channel box function, and the sigma p_2 of the Gaussian. As an example, the fit to one of the anodes is shown in figure 18b. The channel centre positions derived from these fits are listed in table 3. The fitted centre positions to the data from the upper anodes of each channel all agree within 0.05 mm with the fitted positions for the respective lower anodes, indicating that the detector position can be determined within a precision of the same order, which meets the requirements for the horizontal alignment precision.

In the fit of equation 11 to the x-scan data of all eight anodes, the sigma of the convoluted Gaussians were found to be $\sigma = 4.5 \pm 0.1\,\mathrm{mm}$. By simulating x-scans with different beam spots and comparing them to the measurement, it could be verified that a beam profile with this extension would cause the smearing observed in the testbeam data. Therefore, all comparisons of the testbeam data to simulations were performed for simulations with a beam profile of $\sigma = 4.5\,\mathrm{mm}$.

channel	anode	channel centre	anode	channel centre
A	5	(74.12 ± 0.01) mm	6	(74.07 ± 0.01) mm
B	1	(79.45 ± 0.01) mm	2	(79.47 ± 0.01) mm
C	4	(85.54 ± 0.01) mm	7	(85.57 ± 0.01) mm
D	0	(91.10 ± 0.03) mm	3	(91.15 ± 0.02) mm

Table 3: Channel positions fitted to x-scan data, with statistical errors from the fit. The central values for the two anodes per channel agree within 0.05 mm or better with each other. The positions are given in the coordinate system of the movable table's control software.

4.3 Vertical alignment

At the beginning of the testbeam campaign, the position at which the detector was centred with respect to the beam in vertical direction was determined by eye to be at a table position of $y = 76$ mm (in the coordinate system of the steering software for the movable table). To check this estimate, data was taken at different y-positions over a range of 40 mm, with the beam centred between channel C and D. Once the beam moves far enough down from the vertical centre that it enters channel D through the end face rather than the narrow side face, the path length for light production and thus also the amount of detected light will decrease rapidly. The same is true for channel C when the beam entrance point is moved upwards high enough. This effect was used to determine the centre in y-direction by comparing the data to a simulated y-scan. Two parameters need to be adjusted in this comparison: the first is a scaling constant to account for the difference in light yield in data and simulation; the second is an offset in the y-position, i.e. how far the y-axis of the simulation (with the detector centre at position 0 mm) has to be shifted to match the data (with y-positions given in the coordinate system of the table software).

A separate fit was done for both channel C and D. In these fits, both anodes of the respective channel were compared to the simulated y-scan, allowing individual scaling factors for each anode in addition to the common offset in y-direction. Figure 19a shows the data for one channel together with the scaled and shifted simulated y-scans. The fit to the data of channel C returns a vertical centre y-position of $72.5\,\text{mm} \pm 0.1\,\text{mm}$, the fit to channel D a y-position $80.0\,\text{mm} \pm 0.2\,\text{mm}$. The poor agreement is most likely due to large beam spot size of $\sigma = 4.5$ mm. Therefore the distinct edges of the channel edges, which would be the most discriminating factor in the alignment, are washed out. This effect is illustrated in figure 19b, where simulated y-scans for both $\sigma = 0.1$ mm and $\sigma = 4.5$ mm are shown. As another possible explanation a misalignment in the x-z-plane has been considered: The ground plate on which the detector box was standing was only affixed to the movable table on one side, which could allow the whole setup to be tilted around the z-axis. This would induce correlations between the x- and y-coordinate, which would affect channel C and D differently and could lead to different vertical centre positions. However, in the simulation small misalignments in α_z ($\alpha_z < 5°$) were found to have negligible impact on the light yield, and a larger tilt would have been visible by eye.

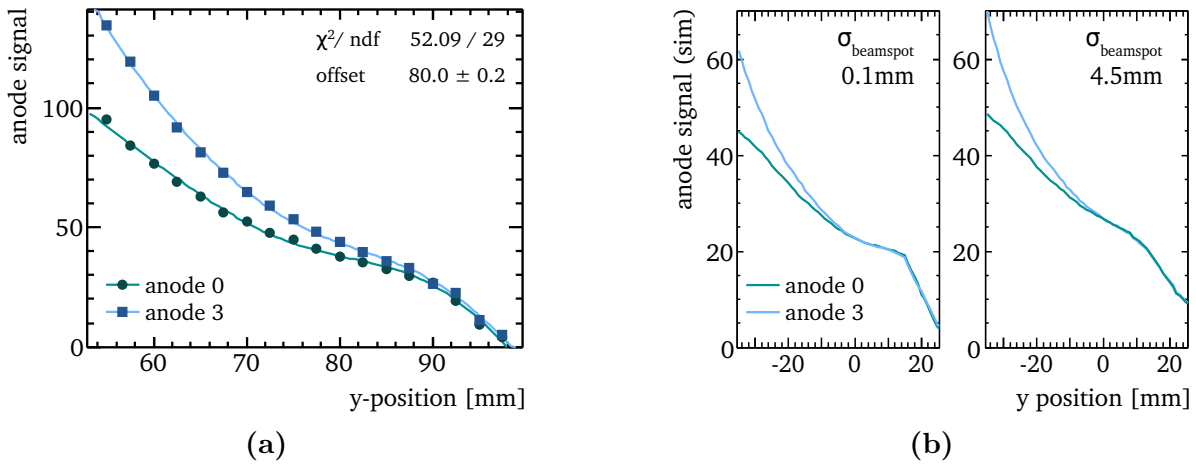

Figure 19: Signal at different y-positions of the detector (a) observed at the testbeam for both anodes of channel D (markers). The solid lines are the fits of a simulated y-scan to the signal of both anodes per channel, with a shift of the y-axis as a free parameter. (b) Simulated y-scans with beam profile $\sigma_{\text{beamspot}} = 0.1\,\text{mm}$ (left) and $\sigma_{\text{beamspot}} = 4.5\,\text{mm}$ (right).

The fit results do nevertheless confirm that the first estimate by eye of a centre at $y_{\text{table}} = 76\,\text{mm}$ was accurate within a few millimetres. Under conditions where the vertical spread of the incident particles is smaller, a better alignment precision is expected.[7]

4.4 Angle scans

The prototype detector was equipped with a stepping motor to change the angle between the incident electron and the detector channels. The angle was calculated from the stepping motor's internal step counter. At the edges of the allowed movement range, a mechanical end switch was located, which stopped the motor movement when it was pressed. In some cases the stepping motor experienced difficulties on leaving the switch, causing a disagreement between the angle calculated from the step counter and the actual angle. This becomes evident by comparing the detector response for individual angle scans taken under otherwise unchanged conditions. Figure 20a shows the signal for both anodes of channel B for two consecutive angle scans, the first one from 30° to 60° (where the end switch was reached), immediately followed the second angle scan back in the opposite direction. In order to reach an agreement between the detector responses, the angle coordinate of the second scan had to be shifted by 1.15°. Three such bi-directional data sets were taken during the testbeam campaign. The angle correction required to obtain the best agreement between opening and closing angle scans for these three data sets were 1.15°, 0.69° and 0.78°, leading to the conclusion that the given angles for the testbeam data are afflicted with an uncertainty of $\mathcal{O}(1°)$.

The data of different angle scans taken during the testbeam campaign were compared to a number of simulated angle scans with different choices for the microfacet distribution

[7] More details on this can be found in [17].

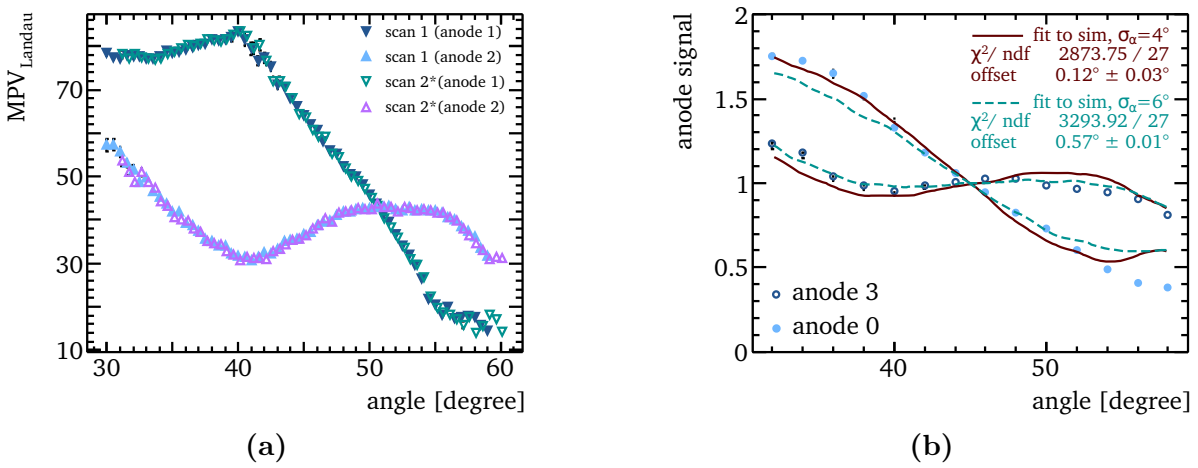

Figure 20: Angular dependence of light yield. (a) Signal for both anodes of channel B for two consecutive angle scans, the first one from 30° to 60° (solid markers), the second one in the opposite direction (open markers). The second scan is shifted by 1.15°. (b) Shape of the angular response function for an angle scan at $y_{\text{table}} = 70\,\text{mm}$, compared to the best-matching simulations at σ_α =4° and σ_α =6°.

parameter σ_α, describing the surface smoothness of the quartz channels, and for the offset in the vertical direction Δy, to study the possibility to determine these parameters from the data: The surface smoothness of the quartz bars used in the prototype detector was not known. For a more polished surface, i.e. a smaller σ_α, more directed reflections occur. Consequently, a change in the incidence angle of the beam is expected to cause larger changes compared to reflections on a rougher surface. The vertical alignment within an uncertainty of several millimetres also had to be taken into account. An offset in the vertical direction moves the central point of the beam crossing by $\frac{\Delta y}{\sin\alpha}$ and therefore affects the detector response especially at small angles.

In order to compare the shape of the detector response in the testbeam data to the different simulations independent of the absolute light yield, the response functions for both data and simulation were normalised to their respective signal at 45°, allowing for a small offset in angle to account for the observed uncertainty in the angle reading for the data discussed above. The current simulation does not describe the angular response satisfactorily for angles $\gtrsim 55°$. To illustrate this, figure 20b shows simulated angle scans with both $\sigma_\alpha = 4°$ and $\sigma_\alpha = 6°$ compared to the data of an angle scan at $y_{\text{table}} = 70\,\text{mm}$. The differences in the shape of the response function hint that additional factors must be present which are not well modelled in the current simulation.
No definite conclusions could be drawn for the vertical offset, since no single value was found to describe the data of several angle scans significantly better than any other. For any given vertical offset, the best agreement was found for $\sigma_\alpha = 5° \pm 1°$. This was the case for all angle scans which were compared to the simulation, leading to the conclusion that a surface smoothness in this range would be a good description of the quartz bars used in the prototype detector.

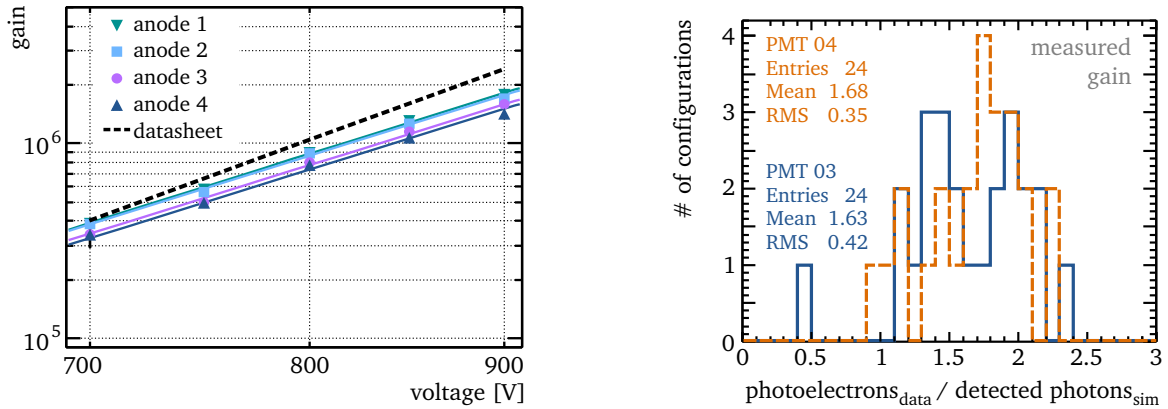

(a) (b)

Figure 21: (a) shows the fitted gain of one of the R7600U04 photomultipliers for different supply voltages, with the dashed line indicating the typical values provided in the datasheet. (b) Ratio between the light yield calculated from the data (using the measured gain) and the number of detected photons predicted by the simulation, for all anodes of both photomultipliers, for measurements at three different incident angles.

4.5 Light yield

In order to compare the light yield observed at the testbeam to the predictions from the simulation, the gain of each photomultiplier anode has to be known. According to the "typical values" from the datasheets, the gain for the R7600U-03 photomultipliers should be twice as high as for the R7600U-04 photomultipliers. In the data however, no discernible difference between the signal of these two photomultiplier types used at the testbeam was found. Therefore, rather than using the datasheet values, a separate test setup was used to determine the actual gain values of the PMTs used with the prototype: inside a light-tight box, a small amount of UV light was produced with an LED and further reduced by a filter mounted in front of the photocathode. A more detailed description of the LED test setup can be found in [14]. The filter strength and LED voltage were chosen such that ≈95 % of the time only the dark current signal was observed.Assuming that the photons reaching the photomultiplier are Poissonian distributed, and that the quantum efficiency can be approximated by a binomial distribution with 20 % probability for detection, this means that in the ≈90 % of the remaining 5 % of the events, in which a signal was observed, this signal stems from a single photon. After subtracting the pedestal, the remaining signal was fitted with a Gaussian to determine the gain. The fitted mean provides the mean number of electrons measured in the QDC, which corresponds to the gain in the single photon case. Data was taken at PMT supply voltages from 700 V to 900 V. The determined gain followed a logarithmic behaviour as expected. As an example, the fitted gain for all four anodes of one of the R7600U-04 photomultipliers is shown in figure 21a.

Once the gain of the photomultipliers is known, the measured QDC signals can be compared to the simulation's predictions for the number of detected photons. For each detector channel, data taken under three different angles (35°, 45°, 55°) with both pho-

tomultiplier types was used for the comparison. For the configuration with the highest light yield, at 35°, summing up the signal for both anodes of a channel yields 107 ± 12 photoelectrons, while the simulation predicts ≈70 photoelectrons for this angle.
The ratio between the observed number of detected photons in the data and the predictions from the simulation, i.e. $\frac{\#\text{photoelectrons}_{\text{data}}}{\#\text{detected photons}_{\text{simulation}}}$, for all configurations are shown in figure 21b. The alignment of the prototype detector at the testbeam with the precisions identified in the previous sections introduces systematic uncertainties in this ratio. While the error on the horizontal alignment is negligible, a systematic uncertainty on the light yield prediction from the simulation of $\frac{\Delta p}{p} = 2\,\%$ for the angular alignment with $\Delta\alpha_x = 1°$ and $\frac{\Delta p}{p} = 10\,\%$ due to the uncertainty of $\mathcal{O}(5\,\text{mm})$ for the vertical alignment have to be considered.

On average, the amount of detected light calculated from the data is higher than expected based on the simulation by a factor of $1.7 \pm 0.4_{(\text{stat.})} \pm 0.2_{(\text{syst.})}$. This might be partly an effect of additional light provided by secondary electrons. In addition to this, a number of assumptions where made in the simulation, such as the roughness of the quartz surface, and the thickness of the optical grease layer. In regard of this, an agreement better than factor 2 between the data and the light yield in the simulation is considered quite satisfactory, especially since the simulation underestimates the amount of light and therefore provides a conservative estimate of the measurable light.

5 Conclusions

Precise polarimetry is crucial for precision measurements at future lepton colliders, such as the International Linear Collider. At the ILC, two Compton polarimeters per beam aim for an accuracy of $\delta\mathcal{P}/\mathcal{P} = 0.25\,\%$, limited by the linearity and the alignment of the baseline gas Cherenkov detectors.

A novel concept for detecting the Compton-scattered electrons using quartz as Cherenkov medium has been developed. Due to its much larger light yield per incident electron, it allows to resolve individual peaks in the measured Cherenkov light corresponding to different numbers of Compton electrons. This concept can improve the systematic uncertainty of the polarisation measurement substantially. In particular, it allows to control non-linearities in the response of the photodetectors used to detect the Cherenkov light, but also aids in alignment of the detector array.

A four-channel prototype detector has been built and operated in a first testbeam campaign. The detector response to single electrons has been measured and compared to the simulation. The light yield per electron, which was a factor of $1.7 \pm 0.4_{(\text{stat.})} \pm 0.2_{(\text{syst.})}$ higher than expected from the simulation, was found to be suitable for the construction of a detector capable of resolving individual peaks in the required dynamic range at the upstream polarimeter of the International Linear Collider.

The testbeam data allowed a horizontal alignment of the prototype detector on the order of 0.05 mm. While the vertical alignment and study of the angular dependence of the detector would benefit from further investigation under better constrained conditions,

i.e. with a smaller beam spot size and a more accurate determination of the vertical alignment independent of the data, they were sufficient to allow to determine that the surface roughness of the quartz used for the prototype is best described by a microfacet parameter $\sigma_\alpha = 5^\circ \pm 1^\circ$. The noise level of the electronic setup at the testbeam was not adequate, leading to a signal width factor 2 larger considered attainable. In the future it is planned to test this prototype with multiple electrons and less noisy electronics to establish that the achieved light yield does indeed allow to resolve individual Compton electrons.

Simulation studies extrapolating the testbeam results to ILC conditions showed that single-peak fitting can compensate photodetector non-linearities up to 4 % and allows a horizontal alignment to about 10 μm. The impact of tilts in the horizontal plane (0.07 %/mrad) stays similar as for the baseline gas detector concept. The non-linearity compensation and improved alignment would reduce the effect of the two leading sources of systematic uncertainties on the polarimeter measurements significantly, to a level comparable to the knowledge of the laser polarisation. This could reduce the total systematic uncertainty to even $\delta\mathcal{P}/\mathcal{P} = 0.20\,\%$, at least in case of the upstream polarimeter. In case of the downstream polarimeter, further studies are needed to investigate whether the low Cherenkov threshold of quartz poses a problem in the harsh background conditions.

Acknowledgement

The construction of the prototype would not have been possible without the great technical support by Volker Prahl, Bernd Beyer and Dörte David. In particular we thank Benno List for fruitful discussions and the encouragement to pursue the idea of single-peak resolution. The results presented here could not be achieved without the National Analysis Facility and testbeam infrastructure at DESY and we thank the NAF and testbeam teams for their continuous support. We thankfully acknowledge the financial support by the BMBF-Verbundforschung in the context of the project "Spin-Management polarisierter Leptonstrahlen an Beschleunigern".

References

[1] G. Moortgat-Pick *et al.*, "The role of polarized positrons and electrons in revealing fundamental interactions at the Linear Collider" 2005, doi:10.1016/j.physrep.2007.12.003.

[2] ILC Technical Design Report, 2013,
`http://www.linearcollider.org/ILC/Publications/Technical-Design-Report`
Volume 1: "Executive Summary", arXiv:1306.6327v1 [physics.ins-det],
Volume 2: "Physics", arXiv:1306.6352v1 [physics.ins-det],
Volume 3.I: "Accelerator R&D", arXiv:1306.6353v1 [physics.acc-ph],
Volume 3.II: "Accelerator Baseline Design", arXiv:1306.6328v1 [physics.acc-ph],
Volume 4: "Detectors", arXiv:1306.6329v1 [physics.ins-det].

[3] S. Boogert *et al.*, "Polarimeters and Energy Spectrometers for the ILC Beam Delivery System", JINST **4**, P10015 (2009), doi:10.1088/1748-0221/4/10/P10015.

[4] J. List [ILD and SiD Collaborations], "Beam Polarisation and Triple Gauge Couplings in $e^+e^- \to W^+W^-$ at the ILC", PoS **EPS-HEP 2013** (2013) 233, http://pos.sissa.it/archive/conferences/180/233/EPS-HEP%202013_233.pdf.

[5] I. Marchesini, "Triple Gauge Couplings and Polarization at the ILC and Leakage in a Highly Granular Calorimeter", PhD Thesis, University of Hamburg, 2011 (DESY-THESIS-2011-044), http://www-library.desy.de/cgi-bin/showprep.pl?desy-thesis-11-044.

[6] A. Rosca, "Measurement of the beam polarisation at the ILC using the WW annihilation data", LC-REP-2013-009, http://www-flc.desy.de/lcnotes/notes/LC-REP-2013-009.pdf.

[7] G. Wilson, "Beam polarization studies with single bosons", presentation at LCWS12 (Arlington, 2012), https://agenda.linearcollider.org/event/5468/session/13/contribution/294.

[8] M. Beckmann, J. List, A. Vauth, and B. Vormwald, "Spin Transport and Polarimetry in the Beam Delivery System of the International Linear Collider", 2014 JINST **9** (2014) P07003, doi:10.1088/1748-0221/9/07/P07003 [arXiv:1405.2156 physics.acc-ph].

[9] C. Bartels, J. Ebert, A. Hartin, C. Helebrant, D. Kaefer and J. List, "Design and Construction of a Cherenkov Detector for Compton Polarimetry at the ILC", JINST **7** (2012) P01019 [arXiv:1011.6314 physics.ins-det].

[10] M. L. Swartz, Phys. Rev. D **58** (1998) 014010 [hep-ph/9711447].

[11] V. Gharibyan, N. Meyners and P. Schuler, "The TESLA Compton Polarimeter", LC-DET-2001-047, 2001, http://www-flc.desy.de/lcnotes/.

[12] K. Abe *et al.* [SLD Collaboration], "A High precision measurement of the left-right Z boson cross-section asymmetry", Phys. Rev. Lett. **84** (2000) 5945, doi:10.1103/PhysRevLett.84.5945 [arXiv:hep-ex/0004026].

[13] K. O. Eyser, C. Helebrant, D. Kaefer, J. List and U. Velte, "Simulation Studies and Detector Scenarios for an ILC Polarimeter" [arXiv:0709.2859 physics.ins-det].

[14] B. Vormwald, "From Neutrino Physics to Beam Polarisation - a High Precision Story at the ILC", PhD Thesis, University of Hamburg, 2014 (DESY-THESIS-2014-006), http://www-library.desy.de/cgi-bin/showprep.pl?thesis14-006.

[15] I. Ben Mordechai, G. Alexander, "A Transverse Polarimeter for a Linear Collider of 250 GeV e^+e^- Beam Energy", LC-M-2012-001, http://www-flc.desy.de/lcnotes/notes/LC-M-2012-001.pdf.

[16] C. Helebrant, "In Search of New Phenomena using Polarization – HERA and ILC", PhD Thesis, University of Hamburg, 2009 (DESY-THESIS-2009-049), http://www-library.desy.de/cgi-bin/showprep.pl?desy-thesis-09-049.

[17] A. Vauth, "A Quartz Cherenkov Detector for Polarimetry at the ILC", PhD Thesis, University of Hamburg, 2014 (DESY-THESIS-2014-022), http://www-library.desy.de/cgi-bin/showprep.pl?thesis14-022.

[18] I. E. Tamm, "General Characteristics of Vavilov-Cherenkov Radiation", Science **131** no. 3395 (1960), 206–210, doi:10.1126/science.131.3395.206.

[19] The GEANT4 Collaboration, "GEANT4 – A Simulation Toolkit", Nucl. Instrum. Meth. A **506**, no. 3 (2003), 250–303; The GEANT4 Collaboration, "GEANT4 Developments and Applications", IEEE Trans. Nucl. Science **53** no. 1 (2006), 270-278; ISSN: 0018–9499.

[20] Heraeus Quarzglas GmbH & Co. KG, "Quartz Glass for Optics: Data and Properties", datasheet (2013), available online at http://optik.heraeus-quarzglas.de/media/webmedia_local/downloads/FusedsilicaandQuartzGlassforOpticsDataandProperties.pdf.

[21] Cargille Laboratories Inc., "Fused Silica Matchng Liquid Code 06350", datasheet (2002), available online at http://www.cargille.com/FS06350.pdf; Cargille Laboratories Inc., "Fused Silica Matchng Liquid Code 50350", datasheet (2002), available online at http://www.cargille.com/FS50350.pdf.

[22] A. Levin and C. Moisan, "A More Physical Approach to Model the Surface Treatment of Scintillation Counters and its Implementation into DETECT", 1996 IEEE Nuclear Science Symp. Conf. Rec (1996), doi:10.1109/NSSMIC.1996.591410.

[23] Hamamatsu Photonics K.K., "Multianode photomultiolier tube R7600U-M4 series", datasheet (2010), available online at `http://www.hamamatsu.com/resources/pdf/etd/R7600U-M4_TPMH1318E02.pdf`.

[24] J. Cohen-Tanugi *et al.*,"Optical properties of the DIRC fused silica Cherenkov radiator", Nucl. Instrum. Meth. A **515**, no. 3 (2003), 680–700; doi:10.1016/j.nima.2003.07.026.

[25] T. Behnke *et al.*, "Test Beams at DESY", EUDET-Memo 2007-11, available online at `http://www.eudet.org/e26/`; see also `http://testbeam.desy.de`.